IEEE Access
Multidisciplinary | Rapid Review | Open Access Journal

Received June 15, 2021, accepted July 15, 2021, date of publication August 16, 2021, date of current version August 26, 2021.

Digital Object Identifier 10.1109/ACCESS.2021.3105296

A Trajectory-Driven 3D Non-Stationary mm-Wave MIMO Channel Model for a Single Moving Point Scatterer

NURILLA AVAZOV, (Member, IEEE), RYM HICHERI, (Member, IEEE), MUHAMMAD MUAAZ, FILIPPO SANFILIPPO, (Senior Member, IEEE), AND MATTHIAS PÄTZOLD, (Senior Member, IEEE)
Faculty of Engineering and Science, University of Agder, 4898 Grimstad, Norway
Corresponding author: Nurilla Avazov (nurilla.avazov@uia.no)

This work was supported by the CareWell Project through the Research Council of Norway under Grant 300638.

ABSTRACT This paper proposes a new non-stationary three-dimensional (3D) channel model for a physical millimeter wave (mm-Wave) multiple-input multiple-output (MIMO) channel. This MIMO channel model is driven by the trajectory of a moving point scatterer, which allows us to investigate the impact of a single moving point scatterer on the propagation characteristics in an indoor environment. Starting from the time-variant (TV) channel transfer function, the temporal behavior of the proposed non-stationary channel model has been analyzed by studying the TV micro-Doppler characteristics and the TV mean Doppler shift. The proposed channel model has been validated by measurements performed in an indoor environment using a MIMO radar kit operating at 24 GHz. For the measurement campaign, we used a single swinging pendulum as a model for a moving point scatterer. The trajectory of the pendulum has been captured by an inertial measurement unit attached to the pendulum and by a motion capture camera system. The measured trajectories are fed into the proposed mm-Wave MIMO channel model. The results obtained for the micro-Doppler characteristics show an excellent agreement between the proposed MIMO channel model and real-world measured channels in the presence of a moving point scatterer. We believe that our model can serve as a basis for the development of novel non-stationary MIMO channel models capturing the effects caused by moving objects and people.

INDEX TERMS MIMO channel, channel measurements, mean Doppler shift, mm-Wave channels, non-stationary channels, multipath propagation, radar, spectrogram, time-frequency analysis.

I. INTRODUCTION

In recent years, millimeter wave (mm-Wave) communications has been proposed as key enabler for the development of the fifth generation (5G) communication systems [1]. Hence, mm-Wave technologies have gained a great attention from both research institutes and industries due to large bandwidth availability, which offers high transmission data rates [2]. In order to exploit important benefits of mm-Wave communications, a detailed knowledge of the corresponding channel propagation is crucial [3]. Mm-Wave radio propagation characteristics differ from channels with sub-6 GHz bands in terms of high path loss, high delay resolution, and blockage caused by humans crossing the line of sight [4]. Therefore, a number of channel models for mm-Wave bands between 6 and 100 GHz have been investigated and developed for various scenarios, such as outdoor [5]–[7], indoor [8]–[11], and vehicle-to-vehicle [12], [13]. For completeness, it should be mentioned that channel models for outdoor propagation scenarios and sub-6 GHz mobile-to-mobile (M2M) communications have also been studied in the literature. In this paper, we focus on the analysis of indoor fixed-to-fixed (F2F) communications considering systems operating in the mm-Wave bands. Therefore, the proposed model differs from M2M communications in a way that the angle-of-departure (AOD) and angle-of-arrival (AOA) of the transmitted wave and the received wave, respectively, are determined by the position of a moving point scatterer and are therefore related

The associate editor coordinating the review of this manuscript and approving it for publication was Matti Hämäläinen.

to each other. In an M2M communication scenarios, however, the AOD and the AOA of the wave incidents are independent random variables. Thus, by using the trajectory of a moving point scatterer, we derive a trajectory-driven channel model.

In [9], a measurement-based spatio-temporal channel model for the 60 and 70 GHz frequency bands has been presented by Haneda *et al.* for indoor environments, such as large office rooms, shopping malls, and stations. It has been shown that the measured spatio-temporal radio channel characteristics of the two frequency bands demonstrate similar behaviour for such environments. Maltsev *et al.* have developed a non-stationary mm-Wave channel model for the 60 GHz frequency band by using a quasi-deterministic modeling approach [14]. The authors have measured power delay profiles of the underlying mm-Wave channel. Rappaport *et al.* [8] have presented indoor and outdoor measurement-based mm-Wave channel models for 28, 38, 60, and 73 GHz frequency bands. In [11], radio propagation measurements of mm-Wave channel characteristics at the 28 GHz frequency band have been presented for in-building environments. The authors have mainly investigated the distribution of scatterers in the considered indoor area.

In practice, an indoor propagation environment induces significant distortions on a signal propagating through that medium. These distortions are caused by multipath propagation and the Doppler effect arising from the motion of people within the indoor space. In this context, designing accurate and reliable channel models is of vital importance for the design and performance analysis of mm-Wave communication systems operating under real-world conditions. Therefore, several studies have been conducted to characterize the propagation delays and Doppler frequencies of the underlying channel. More importantly, propagation characteristics, such as spherical wavefronts, multipath scattering, and time-variant channel properties in space-time-frequency domains need to be thoroughly analyzed.

In general, the level of detail required for channel modeling greatly depends on the system parameters, such as the carrier frequency, the bandwidth, the propagation environment, and the configuration of the transmitter and receiver antennas. Zheng *et al.* [15] mentioned that the channel parameters, such as amplitude, phase, and Doppler frequency shifts, are environment-dependent and their values change with different locations and orientations. Gustafson *et al.* [16] presented a measurement-based multipath clustering channel model for a double-directional multiple-input multiple-output (MIMO) system. They showed that the angular cluster characteristics are related to the geometry of the room. They also discussed the impact of fixed objects on the channel characteristics. The studies in [17] demonstrated that the distribution of the coherence bandwidth depends on the velocity of the moving object and its position with respect to the transmitter antenna.

According to the aforementioned studies, designing channel models, especially for indoor communications under non-stationary conditions, requires a detailed knowledge of the dynamics of the underlying wireless channel characteristics. In the literature, several models have been designed to analyze and represent the time-variant (TV) Doppler characteristics, which are caused by the mobility of moving objects in indoor spaces [18]–[20]. A three-dimensional (3D) non-stationary cluster-based single-input single-output (SISO) channel model has been proposed in [20] for design of human activity recognition systems. In [20], the human body motion has been modelled by a cluster of synchronized moving point scatterers. The authors of [20] have derived expressions for the TV Doppler frequencies by using the TV angles-of-motion (AOM), TV AOA and TV AOD. In [21], a 3D stochastic double-spherical channel model has been developed for mm-Wave MIMO communication systems. To characterize human body motions, a dynamic channel model has been presented in [22], where the human body segments were modelled by using different geometrical shapes, such as cylinders and spheres.

Owing to the Doppler effect, human motion results in temporal changes of the channel characteristics. These changes are usually studied through the spectrogram of the channel and are commonly referred to as micro-Doppler signatures. Theoretical investigations of micro-Doppler signatures require a prior knowledge of the exact time-variant trajectories of the different human body segments, such as head, shoulders, upper arms, lower arms, hands, upper legs, etc. To the best of the authors' knowledge, analytical studies on the kinetic and mechanical modeling of human body motion are limited in the context of channel modeling. In this regard, several studies assume that the human body can be represented by a single point scatterer. A traditional assumption is to consider a spherical object as a single point scatterer, for which analytical expressions for the TV trajectories are available [23]. For example, the estimation and analysis of the micro-Doppler signatures of a slow-moving target have been presented in [24] by using a forward scattering SISO radar system. As a target, the authors considered a swinging pendulum that is placed on a moving trolley. The analysis of the TV Doppler characteristics of a non-stationary channel in the presence of a swinging pendulum, which is attached to the ceiling of the room, can be found in [25] and [26]. In [25], the authors presented a 3D indoor channel model for radio-frequency (RF) sensing. They described the moving object's (pendulum's) trajectory by the TV speed, TV AOM, and the TV elevation AOA. It has been shown that the proposed model allows to describe the channel state information (CSI) of measured RF data, that has been collected by using a commercial Wi-Fi system. In [26], a 3D non-stationary single-input multiple-output (SIMO) channel model has been proposed for the mobility analysis of a single swinging pendulum as a moving point scatterer. The TV spectrogram and the TV mean Doppler shift caused by the motion of the pendulum have been analyzed. The model has been validated by measured data recorded by using radar kit operating at 24 GHz. Special attention has been paid to the impact of the receiver antenna positions on the amplitude of the TV Doppler spectral components.

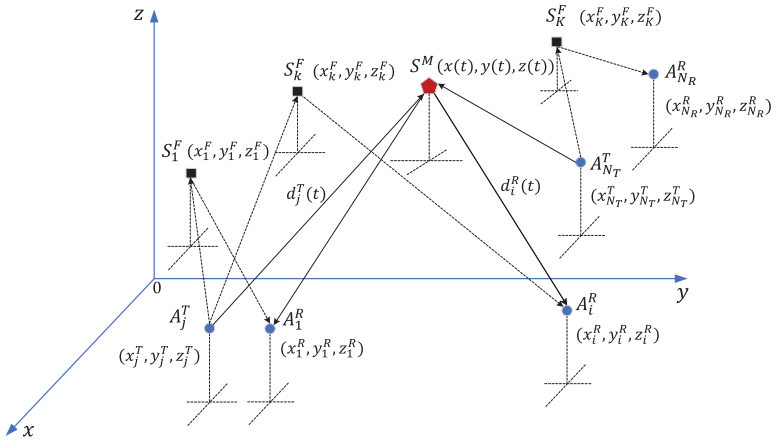

FIGURE 1. 3D geometrical channel model for an $N_T \times N_R$ MIMO system with a single moving scatterer S^M at the TV position $(x(t), y(t), z(t))$ and K fixed scatterers S_k^F at fixed positions (x_k^F, y_k^F, z_k^F) for $k = 1, 2, \ldots, K$.

The goal of this paper is to extend the analysis of a SIMO channel presented in [26] to a MIMO channel model. To this aim, we propose a method for the design of a 3D trajectory-driven non-stationary MIMO channel model for a moving point scatterer in an indoor environment. We investigate the TV micro-Doppler signature of the moving point scatterer for different MIMO links. As a mechanical model for moving point scatterer, we consider a single pendulum swinging in a fixed direction. Hence, the proposed channel model is driven by the trajectory of a swinging pendulum. By considering the trajectory of the pendulum, we derive an analytical expression for the trajectory-driven TV channel transfer function (CTF) and the corresponding complex channel gain of the MIMO system. The input signals of the trajectory-driven MIMO channel model are the TV positions of the swinging pendulum, which can be computed analytically [26]. We analyse the TV Doppler characteristics, such as the spectrograms and the TV mean Doppler shifts of different MIMO links. The theoretical results are validated through real-world measured data. Here, the comparison is made by using three different sets of measured data. Set 1 corresponds to the measured RF channel, which is obtained by using a mm-Wave MIMO radar kit (Ancortek SDR-KIT 2400T2R4) operating at 24 GHz. Set 2 and Set 3 contain the information about the TV trajectory of the moving point scatterer. The data of Set 2 has been recorded by using an inertial measurement unit (IMU) sensor [27], which was attached to the swinging pendulum. On the other hand, the data of Set 3 has been obtained from a motion capture (MOCAP) camera system [28]. In our scenario, the camera system captures the trajectories of the pendulum by using markers attached to the ball. The perfect match between the TV spectrograms of the measured RF signals and those of the proposed trajectory-driven mm-Wave MIMO channel model ascertains the validity of the model and the usefulness of the work.

Considering the MIMO channel, we studied the impact of the antenna positions (MIMO links) on the TV spectrograms and the TV mean Doppler shifts. To the best of our knowledge, the impact of different MIMO links on the micro-Doppler signatures of a moving point scatterer has not been studied yet. In this regard, the main novelties of this paper are as follows:

1) We propose a 3D non-stationary mm-Wave MIMO channel model for a moving object modelled by a point scatterer in indoor environments.
2) We derive analytical expressions for trajectory-driven CTFs and the corresponding complex channel gains.
3) We investigate the impact of the antenna positions on the TV Doppler spectrogram and the TV mean Doppler shift.
4) We demonstrate the correctness of the concept by validating the proposed trajectory-driven channel model using measured RF data, IMU data, and MOCAP data.
5) We present a framework for pre- and post-processing of RF, IMU, and MOCAP measurement data sets.
6) We perform a qualitative and quantitative analysis to evaluate the accuracy of the proposed model.

The remaining part of the paper is structured as follows. Section II presents a 3D geometrical MIMO channel model for an indoor environment with a single moving scatterer and K fixed scatterers. The proposed trajectory-driven channel model and the spectrogram analysis are presented in Section III and Section IV, respectively. The measurement and numerical results are provided in Section V. Finally, the conclusion is drawn in Section VI.

II. 3D INDOOR GEOMETRICAL CHANNEL MODEL

In this section, we present a 3D indoor geometrical channel model for the propagation scenario illustrated in Fig. 1. The propagation scenario consists of N_T fixed transmitter antennas A_j^T $(j = 1, 2, \ldots, N_T)$, N_R fixed receiver antennas A_i^R $(i = 1, 2, \ldots, N_R)$, a moving scatterer S^M, and K fixed scatterers S_k^F $(k = 1, 2, \ldots, K)$. The jth transmitter antenna A_j^T and the ith receiver antenna A_i^R are set at the predefined positions (x_j^T, y_j^T, z_i^T) and (x_i^R, y_i^R, z_i^R), respectively. A moving point

scatterer S^M is depicted in Fig. 1 by a red pentagon, which has the TV coordinates $x(t)$, $y(t)$, and $z(t)$ describing the 3D trajectory $\mathcal{C}(t) = (x(t), y(t), z(t))$. We assume single-bounce scattering and non-line of sight conditions. As shown in Fig. 1, we denote by $d_j^T(t)$ the Euclidean distance between the moving scatterer S^M and the jth transmitter antenna A_j^T, whereas $d_i^R(t)$ stands for the Euclidean distance between the ith receiver antenna A_i^R and the moving scatterer S^M. The distances $d_j^T(t)$ and $d_i^R(t)$ can be expressed in terms of the TV coordinates $x(t)$, $y(t)$, and $z(t)$ of S^M as

$$d_j^T(t) = \sqrt{(x(t)-x_j^T)^2 + (y(t)-y_j^T)^2 + (z(t)-z_j^T)^2} \quad (1)$$

$$d_i^R(t) = \sqrt{(x(t)-x_i^R)^2 + (y(t)-y_i^R)^2 + (z(t)-z_i^R)^2}. \quad (2)$$

In the propagation scenario, we also consider multiple stationary objects, such as furniture, decoration items, and walls, which are modelled by K fixed scatterers S_k^F ($k = 1, 2, \ldots, K$) as depicted in Fig. 1. The position of the kth fixed scatterer is denoted by (x_k^F, y_k^F, z_k^F). Analogously to (1) and (2), the Euclidean distance between the fixed scatterer S_k^F and the jth (ith) transmitter (receiver) antenna is denoted by $d_{j,k}^T$ ($d_{i,k}^R$) and given by

$$d_{j,k}^T = \sqrt{(x_k^F - x_j^T)^2 + (y_k^F - y_j^T)^2 + (z_k^F - z_j^T)^2} \quad (3)$$

and

$$d_{i,k}^R = \sqrt{(x_k^F - x_i^R)^2 + (y_k^F - y_i^R)^2 + (z_k^F - z_i^R)^2} \quad (4)$$

respectively.

III. MIMO CHANNEL MODEL

In this section, we present the TV-CTF of the $N_T \times N_R$ MIMO channel. As depicted in Fig. 1, the radio waves travel from the jth transmitter antenna A_j^T to the moving (fixed) scatterer S^M (S_k^F) and impinges at the ith receiver antenna A_i^R. Hence, the TV-CTF $H_{i,j}(t, f')$ of the link from A_j^T to A_i^R can be presented as:

$$H_{i,j}(t, f') = H_{i,j}^M(t, f') + \sum_{k=1}^{K} H_{i,j,k}^F(f') \quad (5)$$

where $H_{i,j}^M(t, f')$ and $H_{i,j,k}^F(f')$ stand for the components caused by the moving scatterer S^M and the kth fixed scatterer S_k^F, respectively. The TV-CTF determined by the moving scatterer S^M can be expressed as

$$H_{i,j}^M(t, f') = c_{i,j}^M e^{j[\theta_{i,j}^M - 2\pi(f'+f_c)\tau_{i,j}^{'M}(t)]}. \quad (6)$$

where $c_{i,j}^M, f_c, \theta_{i,j}^M$, and $\tau_{i,j}^{'M}(t)$ denote a fixed path gain, a carrier frequency, a phase, and a TV propagation delay of the moving point scatterer. respectively. The second term of (5) can be expressed as

$$H_{i,j,k}^F(f') = c_{i,j,k}^F e^{j[\theta_{i,j,k}^F - 2\pi(f'+f_c)\tau_{i,j,k}^{'F}]}. \quad (7)$$

Analogously, the TV-CTF $H_{i,j,k}^F(f')$ of the kth fixed scatterer is determined by a fixed path gain $c_{i,j,k}^F$, a phase $\theta_{i,j,k}^F$ and a propagation delay $\tau_{i,j,k}^{'F}$ associated with the kth fixed scatterer. It is worth noting that both phases $\theta_{i,j}^M$ and $\theta_{i,j,k}^F$ in (6) and (7), respectively, are modelled as independent and identically distributed (i.i.d.) random variables, each of them following a uniform distribution over the interval from $-\pi$ to π. The TV propagation delay $\tau_{i,j}^{'M}(t)$ of the radio wave travelling from the jth transmitter antenna A_j^T to the ith receiver antenna A_i^R via the moving point scatterer S^M can be computed in terms of the Euclidean distances $d_j^T(t)$ and $d_i^R(t)$ as follows

$$\tau_{i,j}^{'M}(t) = \frac{d_j^T(t) + d_i^R(t)}{c_0} \quad (8)$$

where c_0 denotes the speed of light. Similarly, the time-invariant propagation delays $\tau_{i,j,k}^{'F}$ of the wave propagating from the jth transmitter antenna A_j^T to the ith receiver antenna A_i^R via the fixed scatterer S_k^F can be computed in terms of the Euclidean distances $d_{j,k}^T$ and $d_{i,k}^R$ as

$$\tau_{i,j,k}^{'F} = \frac{d_{j,k}^T + d_{i,k}^R}{c_0}. \quad (9)$$

The TV Doppler shift corresponding to the link from A_j^T to A_i^R can be obtained by computing the derivative $\dot{\tau}_{i,j}^{'M}(t)$ of the TV delay $\tau_{i,j}^{'M}(t)$ as follow [25]:

$$f_{i,j}^M(t) = -f_c \dot{\tau}_{i,j}^{'M}(t). \quad (10)$$

IV. SPECTROGRAM ANALYSIS

In this section, we present the spectrogram capturing the effect of a single moving point scatterer. From the spectrogram, we can compute the TV mean Doppler shift. The TV Doppler spectrogram of the communication link between A_j^T and A_i^R is denoted by $S_{i,j}(f, t)$. The computation of the TV Doppler spectrogram $S_{i,j}(f, t)$ of the complex TV-CTF $H_{i,j}^M(t, f')$ determined by the moving scatterer S^M is performed in the following five steps. First, the channel impulse response $h_{i,j}^M(t, \tau')$ is computed by taking the inverse Fourier transform of $H_{i,j}^M(t, f')$ with respect to frequency f' as follows

$$h_{i,j}^M(t, \tau') = \int_{-B/2}^{B/2} H_{i,j}^M(t, f') \exp\left(j2\pi f'\tau'\right) df'. \quad (11)$$

In the second step, we compute the complex channel gain $\mu_{i,j}(t)$ representing the channel link from A_j^T to A_i^R by integrating $h_{i,j}^M(t, \tau')$ over τ' from 0 to the maximum propagation delay $\tau'_{\max}$, i.e.,

$$\mu_{i,j}(t) = \int_0^{\tau'_{\max}} h_{i,j}^M(t, \tau') d\tau' \quad (12)$$

$$\approx c_{i,j}^M e^{j\left[\theta_{i,j}^M - 2\pi f_c \tau_{i,j}^{'M}(t)\right]}. \quad (13)$$

In the third step, the complex channel gain $\mu_{i,j}(t)$ is multiplied by a sliding window function $w(t)$, which is a positive

even function with normalized energy, as follows

$$x_{i,j}(t', t) = \mu_{i,j}(t)w(t' - t). \tag{14}$$

For the sliding window function, we use the Kaiser window function that is given by

$$w(t) = \begin{cases} \dfrac{I_0\left\{\beta\sqrt{1-\left(\frac{2t}{T_0}-1\right)^2}\right\}}{I_0(\beta)}, & 0 \le t \le T_0 \\ 0, & \text{otherwise} \end{cases} \tag{15}$$

where T_0 is the length of the window, and β is parameter that controls the shape of the window function. The symbol $I_0(\cdot)$ stands for the modified Bessel function of the first kind of zero order. In the fourth step, we compute the short-time Fourier transform (STFT) of the signal $x_{i,j}(t', t)$ in (14) with respect to t', i.e.,

$$X_{i,j}(f, t) = \int_{-\infty}^{\infty} x_{i,j}(t', t)e^{-i2\pi ft'}dt'. \tag{16}$$

Finally, by computing the squared magnitude of the STFT $X_{i,j}(f, t)$ in (16), we obtain the TV Doppler spectrogram of the link from A_j^T to A_i^R as

$$S_{i,j}(f, t) = |X_{i,j}(f, t)|^2. \tag{17}$$

By computing the first moment of the TV Doppler spectrogram $S_{i,j}(f, t)$ in (17), we obtain the TV mean Doppler frequency $B^{(1)}_{\mu_{i,j}}(t)$. Hence, the TV mean Doppler shift can be formulated as [25]

$$B^{(1)}_{\mu_{i,j}}(t) = \frac{\int_{-\infty}^{\infty} fS_{i,j}(f, t)df}{\int_{-\infty}^{\infty} S_{i,j}(f, t)df}. \tag{18}$$

Alternatively, the TV mean Doppler shift of the proposed trajectory-driven channel model can also be computed by using the TV Doppler shifts $f^M_{i,j}(t)$ of the corresponding moving point scatterer S^M as follows [25]

$$B^{(1)}_{f^M_{i,j}}(t) = \frac{(c^M_{i,j})^2 f^M_{i,j}(t)}{(c^M_{i,j})^2 + \sum_{k=1}^{K}(c^F_{i,j,k})^2}. \tag{19}$$

V. MEASUREMENTS AND NUMERICAL RESULTS

This section presents the measurement setup for capturing the trajectory of a moving point scatterer in an indoor environment. The analyses of the results obtained from the measurements and the analytical model are also discussed. The indoor propagation environment is a room with a width of 6 m, length of 11.5 m, and height of 2.5 m. In the room, there exist fixed objects, such as chairs, tables, boards, and computers and a moving point scatterer. As a point scatterer, we consider a single swinging pendulum, which is a medicine ball weighing 3 kg. We attach the pendulum to the ceiling of the laboratory room by using a rope with length $L = 1.52$ m. From the geometrical representation of the swinging pendulum shown in Fig. 3, we can compute the trajectory (displacements) $x(t)$, $y(t)$, and $z(t)$ of the pendulum as follows [26]:

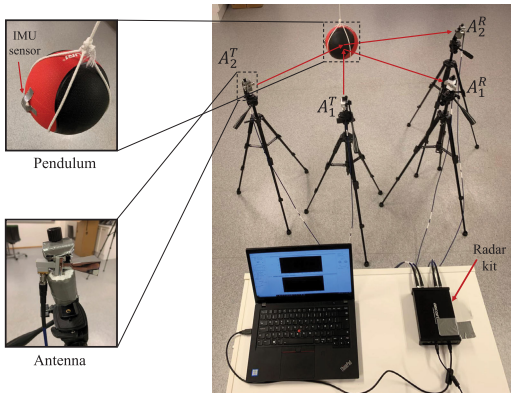

FIGURE 2. Propagation environment used for experimental setup with a radar sensing system and IMU.

$$x(t) = L\sin\left(\arcsin\left(\frac{x_{\max}}{L}\right)\cos\left(\sqrt{\frac{g}{L}}t\right)\right) \tag{20}$$

$$y(t) = 0 \tag{21}$$

$$z(t) = L\left\{1 - \cos\left[\arcsin\left(\frac{x(t)}{L}\right)\right]\right\}, \tag{22}$$

where g and $x_{\max}$ represent the gravity acceleration and the maximum displacement in x-direction, respectively. The TV positions $x(t)$, $y(t)$, and $z(t)$ characterize the TV trajectory of the pendulum $\mathcal{C}(t) = (x(t), y(t), z(t))$. The TV trajectory $\mathcal{C}(t)$ is the input signal of the trajectory-driven channel model, which we refer hereafter as the analytical model. Starting from the mathematical trajectory $\mathcal{C}(t)$ (pendulum model), we can compute the TV spectrogram $S_{i,j}(t, f)$ as outlined in Section IV and depicted in Fig. 4(a).

A. MEASUREMENT SCENARIO FOR RADAR SENSING

The mobility of the pendulum is captured with the MIMO radar sensing system SDR-KIT 2400T2R4 from Ancortek operating at 24 GHz. The radar system has two transmitter and four receiver directional antennas. The transmitted chirp signals have a bandwidth of 250 MHz with 1 ms chirp duration. While employing a full MIMO setup, i.e., 2×4 antenna configurations, we experience a mixture of micro-Doppler signature patterns of the swinging pendulum corresponding to several MIMO sub-links. To avoid this subchannel co-interference, we used only the 2×2 MIMO configuration, in which this mixture of patterns is not negligible. Moreover, to reduce the impact of the subchannel co-interference, we subtracted the TV spectrograms of different links from each other as follows:

$$\check{S}_{1,1}(f, t) = \hat{S}_{1,1}(f, t) + \alpha\hat{S}_{2,1}(f, t) \tag{23}$$

$$\check{S}_{2,1}(f, t) = \hat{S}_{2,1}(f, t) + \beta\hat{S}_{1,1}(f, t) \tag{24}$$

$$S^{\star}_{1,1}(f, t) = \check{S}_{1,1}(f, t) - \check{S}_{2,1}(f, t) \tag{25}$$

where $\check{S}_{1,1}(f, t)$ ($\check{S}_{2,1}(f, t)$) represents the TV spectrograms of the link $A_1^T - A_1^R$ ($A_1^T - A_2^R$) consisting of the patterns of

spectrograms from the other link $A_1^T - A_2^R$ ($A_1^T - A_1^R$). The symbols α and β are weighting factors associated with the spectrograms of the interfering subchannel. Thus, we compute the TV spectrogram of the desired $A_1^T - A_1^R$ link $S^{\star}_{1,1}(f,t)$ as follows

$$S^{\star}_{1,1}(f,t) = \hat{S}_{1,1}(f,t)(1-\beta) + \hat{S}_{2,1}(f,t)(\alpha - 1). \quad (26)$$

If α and β are very small compared to 1, i.e., $\alpha \ll 1$ and $\beta \ll 1$, then we can write

$$S^{\star}_{1,1}(f,t) \approx \hat{S}_{1,1}(f,t) - \hat{S}_{2,1}(f,t). \quad (27)$$

As $\hat{S}_{1,1}(f,t) \geq 0$ and $\hat{S}_{2,1}(f,t) \geq 0$ are in general different, we can set $S^{\star}_{1,1}(f,t)$ to zero for all values of f and t for which the difference in (27) is negative. Thus, we obtain

$$S^{\star}_{1,1}(f,t) \approx \hat{S}_{1,1}(f,t). \quad (28)$$

The same approach can be applied on the other links, which results in $S^{\star}_{2,1}(f,t) \approx \hat{S}_{2,1}(f,t)$, $S^{\star}_{1,2}(f,t) \approx \hat{S}_{1,2}(f,t)$, and $S^{\star}_{2,2}(f,t) \approx \hat{S}_{2,2}(f,t)$. To form communication distinct links, we placed the antennas in a distributed manner as shown in Fig. 2. The antennas are connected to the radar kit with cables of length 3 m each. The transmitter and the receiver antennas are set at the positions (x_j^T, y_j^T, z_j^T) and (x_i^R, y_i^R, z_i^R), respectively, as illustrated in Fig. 3. The coordinates of the antennas and pendulum parameters, such as the maximum displacement $x_{\max}$, and the length of the rope L are listed in Table 1. The emitted waves from the jth transmitter antenna will encounter the pendulum, and the scattered waves impinge at the ith receiver antenna. Subsequently, the received signals are stored and processed for further analysis. Then, we analyse the TV Doppler spectrogram of each link as illustrated in Fig. 4(d).

B. TRAJECTORY CAPTURING BY USING THE IMU

To obtain measurement of the pendulum trajectory, we use MetaMotionR sensor fusion [27]. The IMU sensor is attached to the swinging pendulum as shown in Fig. 2. By using a smartphone, we control the IMU and record the data files via Bluetooth. The data files contain quaternions and linear accelerations of the pendulum. They are applied to compute the Euler angles to rotate the linear accelerations as shown in Fig. 4(b). Then, we have employed a quadratic regression method to smooth the rotated linear accelerations. Thereafter, we have computed the velocities and the trajectory (positions) by integrating linear accelerations. Due to an experimental error, there are linear and quadratic drifts in the velocity and the trajectory. These drifts have been compensated by using the zero-update (ZUPT) algorithm [29]. The TV drift-free horizontal displacement $x(t)$ and the vertical displacement $z(t)$ of the recorded data from the IMU are compared with those of the pendulum model given in (20) and (22), respectively. It is worth noting that to fit the displacements of the IMU data to those of the pendulum model, it is required to calibrate the IMU data by shifting and scaling the graphs in both axes. In our analysis, we have normalized the trajectories obtained from the IMU data as follows

$$\tilde{x}(t) = \frac{\max\limits_t(x(t))}{\max\limits_t(x_{\text{IMU}}(t))} x_{\text{IMU}}(t) \quad (29)$$

$$\tilde{y}(t) = 0 \quad (30)$$

$$\tilde{z}(t) = \frac{\max\limits_t(z(t))}{\max\limits_t(z_{\text{IMU}}(t))} z_{\text{IMU}}(t). \quad (31)$$

Alternatively, the $z(t)$ displacement can be computed by using the $x(t)$ displacement of the IMU data by means of the relationship in (22). However, this is only true if an analytical solution (a mathematical model) is known. Therefore, it is important to develop a channel model that can be used as a reference model to replicate the real channel. Thus, the final obtained (normalized) trajectory $\tilde{C}(t) = (\tilde{x}(t), \tilde{y}(t), \tilde{z}(t))$ will be used as the input signal of the IMU data-driven channel model and to compute its corresponding TV micro-Doppler signatures $\tilde{S}_{i,j}(f,t)$ as illustrated in Fig. 4(b).

TABLE 1. Parameters of the measurement setup.

Model Parameters	Values and Units
(x_1^T, y_1^T, z_1^T)	(1, 0, 1.08) m
(x_2^T, y_2^T, z_2^T)	(0.707, -0.707, 1.08) m
(x_1^R, y_1^R, z_1^R)	(0.707, 0.707, 1.08) m
(x_2^R, y_2^R, z_2^R)	(0, 1, 1.08) m
L	1.52 m
$x_{\max}$	0.55 m

C. TRAJECTORY MEASUREMENTS USING A MOTION CAPTURE (MOCAP) CAMERA SYSTEM

To validate the correctness of the proposed channel model, we also recorded the trajectory of the swinging pendulum by using the MOCAP camera system. The adopted MOCAP camera system is based on the Qualisys capture system [30]. This MOCAP system features the highest-performing technology that is currently available on the market. The setup of the Qualisys MOCAP system is shown in Fig. 5, where 8 Miqus hybrid cameras are used. The Miqus hybrid cameras allow us to capture the mobility of the object by using either a marker-based tracking or a marker-less tracking system. The Miqus hybrid cameras [31] are dual mode cameras capable of streaming full high definition (HD) color video at 85 frames per second or streaming marker data at 340 frames per second. In our preliminary experiment, a collection of MOCAP data is conducted by using Qualisys Track Manager (QTM) [32] based on a marker tracking system. The tracking can be performed in real-time or by post-processing. In the proposed experiment, markers have been placed on the swinging pendulum. Based on the selected markers, a virtual reference frame is established in the center of mass (CoM) of the medicine ball. The QTM's advanced 3D six-degree of freedom (6DOF) tracker computes 3D and

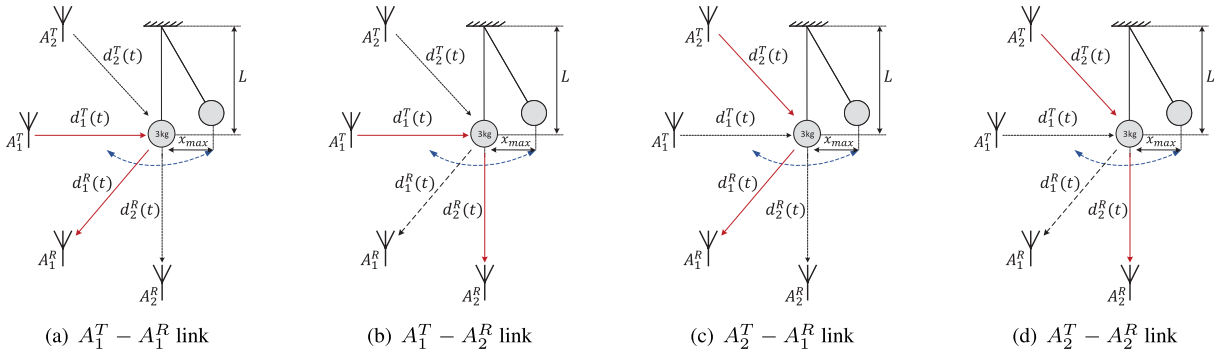

FIGURE 3. Geometrical representations of the MIMO links: (a) $A_1^T - A_1^R$, (b) $A_1^T - A_2^R$, (c) $A_2^T - A_1^R$, and (d) $A_2^T - A_2^R$, respectively.

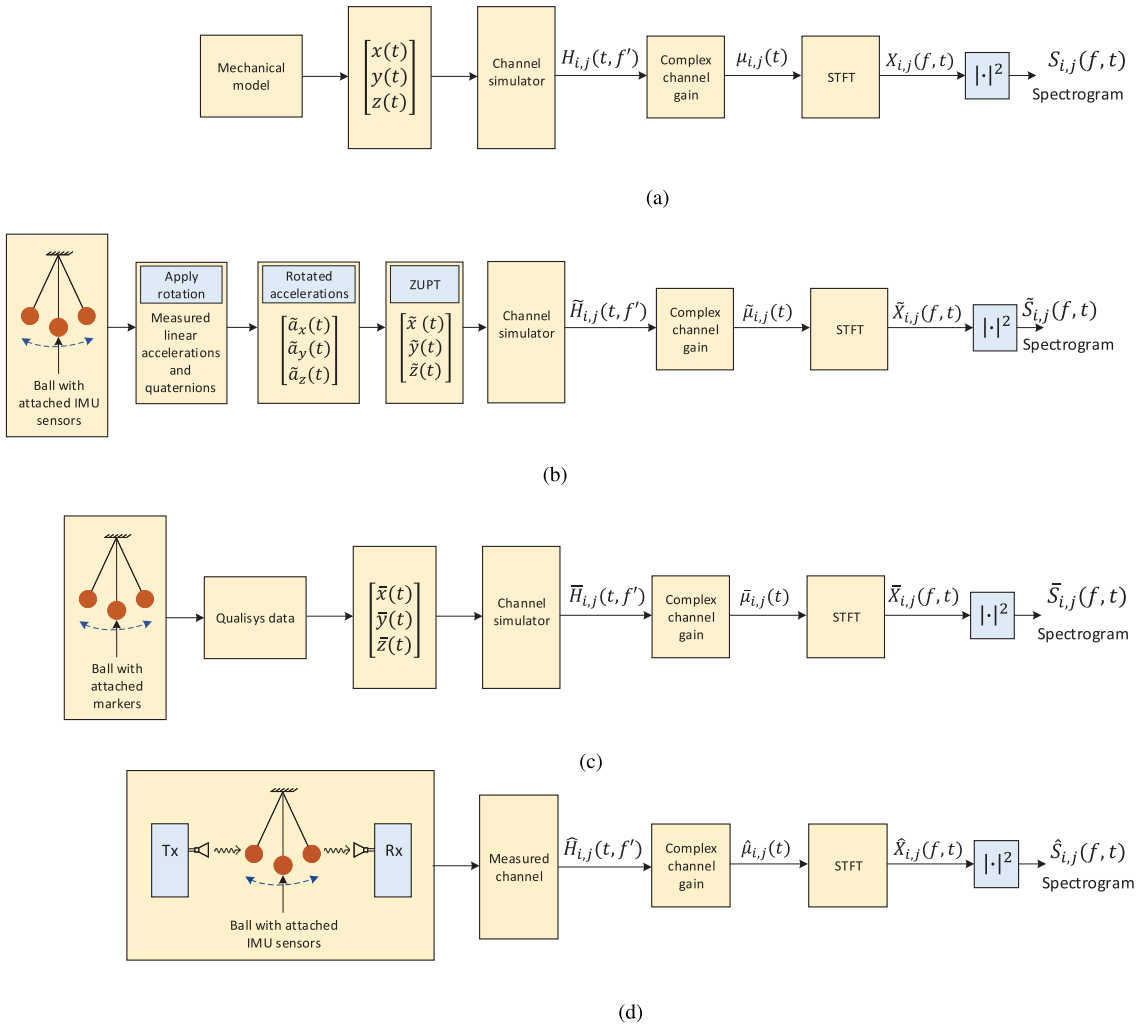

FIGURE 4. Block diagrams demonstrating the steps to compute the spectrograms $S_{i,j}(f,t)$, $\tilde{S}_{i,j}(f,t)$, $\bar{S}_{i,j}(f,t)$, and $\hat{S}_{i,j}(f,t)$ of the (a) analytical model, (b) IMU data-driven model, (c) Qualisys (MOCAP) data-driven model, and (d) measured channel, respectively.

6DOF data by using two-dimensional (2D) data points with minimal latency. Thus, the obtained trajectory of the pendulum $\bar{C}(t) = (\bar{x}(t), \bar{y}(t), \bar{z}(t))$ will be used to compute the MOCAP data-driven channel model. For reasons of comparison, we can then compute TV micro-Doppler signature $\bar{S}_{i,j}(f,t)$, as shown in Fig. 4(c).

Finally, by using the TV micro-Doppler signature, we can obtain the TV mean Doppler shift. We conducted another experiment with the swinging pendulum by using simultaneously the IMU sensor, the MOCAP camera system, and the radar kit configured for the SISO communication link. To investigate the performance of the MOCAP camera

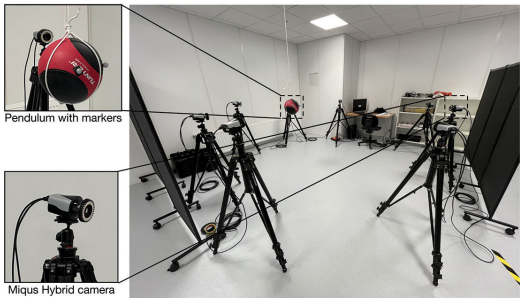

FIGURE 5. Propagation environment used for experimental setup with a MOCAP system and IMU.

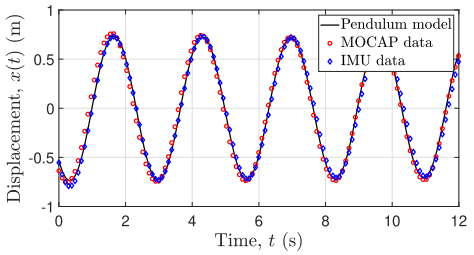

FIGURE 6. TV $x(t)$ displacements of the mechanical model, the measured IMU data, and the MOCAP data.

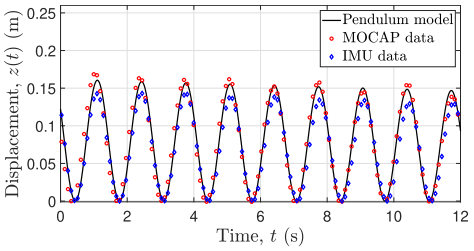

FIGURE 7. TV $z(t)$ displacements of the mechanical model, the measured IMU data, and the MOCAP data.

	Mechanical model data	Qualisys data	Normalized IMU data
Mechanical model data	100	88.56	84.22
Qualisys data	88.71	100	84.98
Normalized IMU data	83.98	84.54	100

FIGURE 8. Similarity score (in %) of the $x(t)$ displacement of the mechanical model, the measured IMU data, and the MOCAP data.

system, we computed the TV-CTF $\bar{H}_{i,j}(t, f')$ and its corresponding mean Doppler shift $\bar{B}^{(1)}_{H_{i,j}}(t)$ by using the trajectory obtained from the MOCAP data.

Figures 6 and 7 illustrate $x(t)$ and $z(t)$ displacements obtained from the mechanical model, the MOCAP data, and the IMU data. We can see that all models match well and demonstrate a good agreement. To investigate the accuracy of the conducted data, we computed a similarity score between the mechanical model and the recorded data. The similarity

	Mechanical model data	Qualisys data	Normalized IMU data
Mechanical model data	100	86.14	79.68
Qualisys data	86.2	100	79.75
Normalized IMU data	76.98	76.95	100

FIGURE 9. Similarity score (in %) of the $z(t)$ displacement of the mechanical model, the measured IMU data, and the MOCAP data.

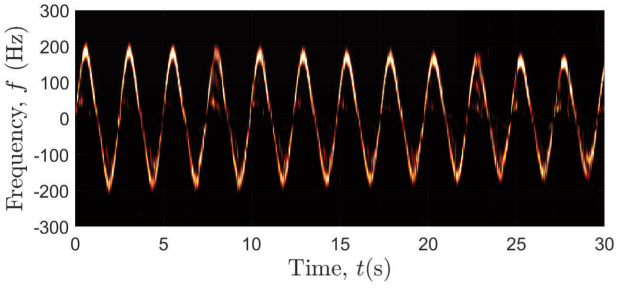

(a)

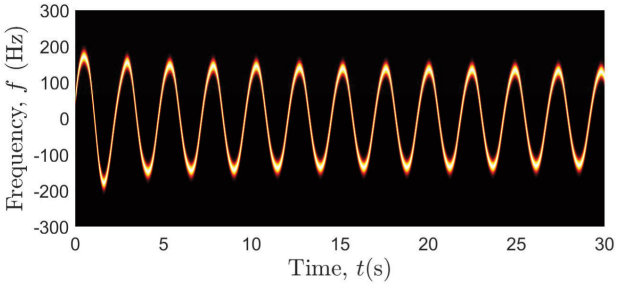

(b)

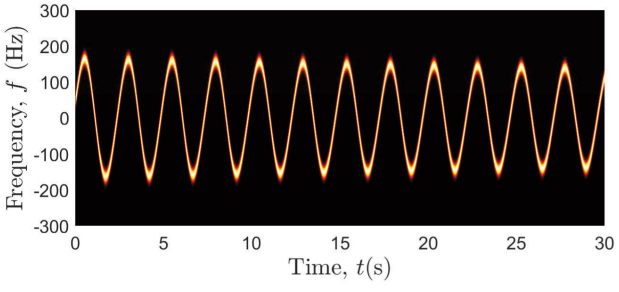

(c)

FIGURE 10. Spectrograms $\hat{S}_{1,1}(f,t)$, $\tilde{S}_{1,1}(f,t)$, and $S_{1,1}(f,t)$ of the (a) measured channel, (b) IMU data-driven channel, and (c) analytical model, respectively, for the A_1^T–A_1^R link.

score can be obtained by using

$$\eta = \left[1 - \frac{\left\|\vec{a}^{\star} - \vec{a}\right\|}{\left\|\vec{a}^{\star}\right\|}\right] 100\% \tag{32}$$

where $\vec{a}^{\star}$ and $\vec{a}$ stand for the measured and analytical data, respectively. By replacing $\vec{a}^{\star}$ and $\vec{a}$ with $x(t)$ and $\tilde{x}(t)$, respectively, we can compute the similarity score between

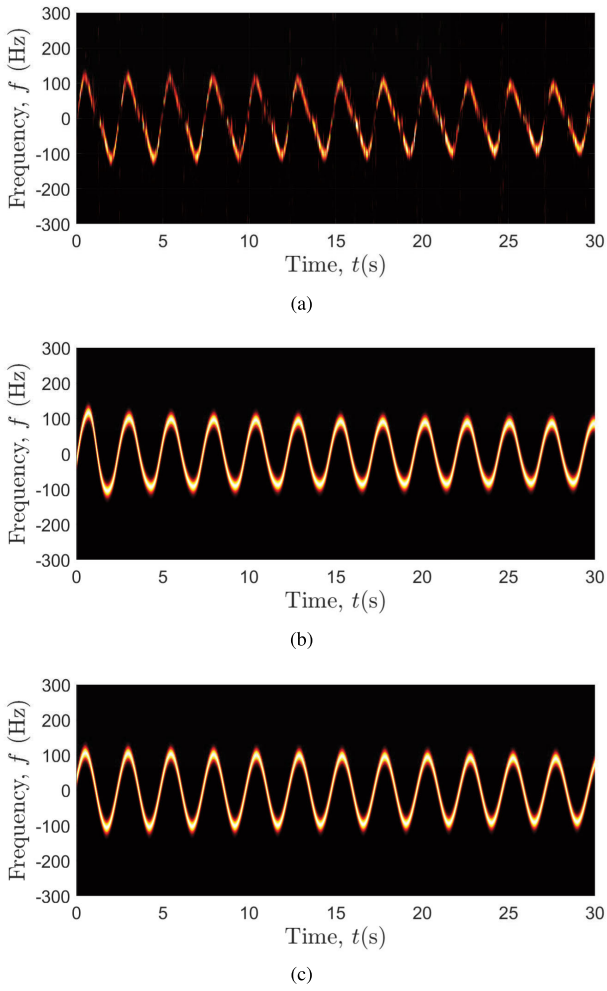

FIGURE 11. Spectrograms $\hat{S}_{2,1}(f,t)$, $\tilde{S}_{2,1}(f,t)$, and $S_{2,1}(f,t)$ of the (a) measured channel, (b) IMU data-driven model, and (c) analytical model, respectively, for the A_1^T–A_2^R link.

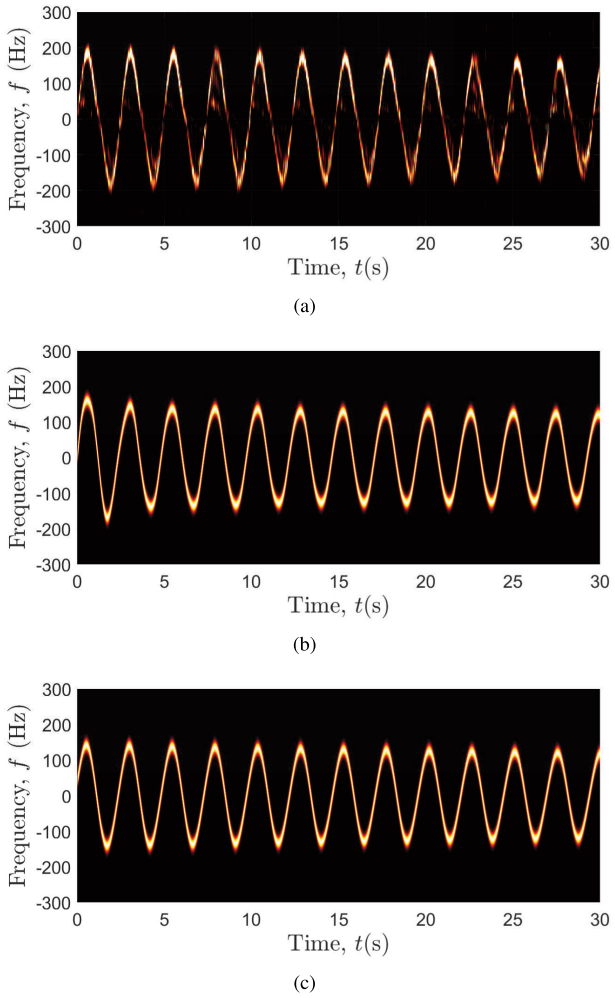

FIGURE 12. Spectrograms $\hat{S}_{1,2}(f,t)$, $\tilde{S}_{1,2}(f,t)$, and $S_{1,2}(f,t)$ of the (a) measured channel, (b) IMU data-driven model, and (c) analytical model, respectively, for the A_2^T–A_1^R link.

the displacements of the mechanical (pendulum) model and the recorded trajectories. Hence, the similarity score of the displacements $x(t)$ and $z(t)$ obtained from the MOCAP data, the IMU data, and the mechanical model can be seen in Figs. 8 and 9. We can observe that the MOCAP data obtained from the QTM system outperforms the one of the IMU data when comparing to the mechanical (pendulum) model.

D. TV SPECTROGRAM AND MEAN DOPPLER SHIFT

The TV spectrograms for the MIMO links A_1^T–A_1^R, A_1^T–A_2^R, A_2^T–A_1^R, and A_2^T–A_2^R are shown in Figs. 10, 11, 12, and 13, respectively. The TV spectrograms of the measured channel $\hat{S}_{i,j}(f,t)$, the IMU data-driven channel $\tilde{S}_{i,j}(f,t)$, and the analytical channel model $S_{i,j}(f,t)$ for the link $A_1^T - A_1^R$ are demonstrated in Figs. 10(a), 10(b), and 10(c), respectively. From a comparison of the results shown in Figs. 10(a)−10(c), we can observe an excellent agreement between the TV micro-Doppler signatures of the measured channel, the IMU-driven channel, and the analytical channel model. The Doppler frequency has positive (negative) values, when the pendulum swings towards (away from) the transmitter antenna A_1^T. When the swinging pendulum reaches its local minimum and maximum displacements as shown in Figs. 6 and 7, then its speed of motion reaches 0 m/s. Hence, the TV Doppler frequency corresponding to the motion of the pendulum approaches 0 Hz. Similar, observations can be seen in Figs. 11, 12, and 13 for the links $A_1^T - A_2^R$, $A_2^T - A_1^R$, and $A_2^T - A_2^R$, respectively. From the results in Figs. 10−13, the impact of the transmitter and the receiver antenna positions on the spectrograms in terms of the amplitude of the Doppler frequency can be seen. In fact, the wave travel distance has an impact on the corresponding propagation delay, which is directly related to the Doppler shift.

We have also investigated the TV mean Doppler shifts $\hat{B}_{i,j}^{(1)}(t)$, $\tilde{B}_{i,j}^{(1)}(t)$, and $B_{i,j}^{(1)}(t)$ of the measured channel, the IMU-driven channel, and the analytical channel models, respectively. In Figs. 14−17, we have illustrated the TV mean Doppler shifts for the different MIMO links. Similar to

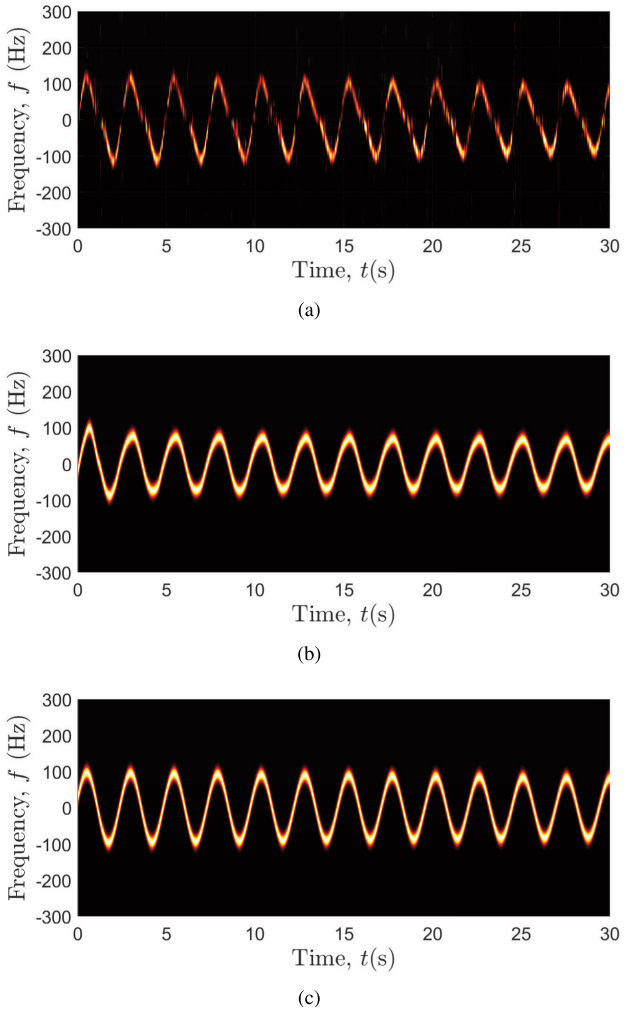

FIGURE 13. Spectrograms $\hat{S}_{2,2}(f,t)$, $\tilde{S}_{2,2}(f,t)$, and $S_{2,2}(f,t)$ of the (a) measured channel, (b) IMU data-driven model, and (c) analytical model, respectively, for the A_2^T–A_2^R link.

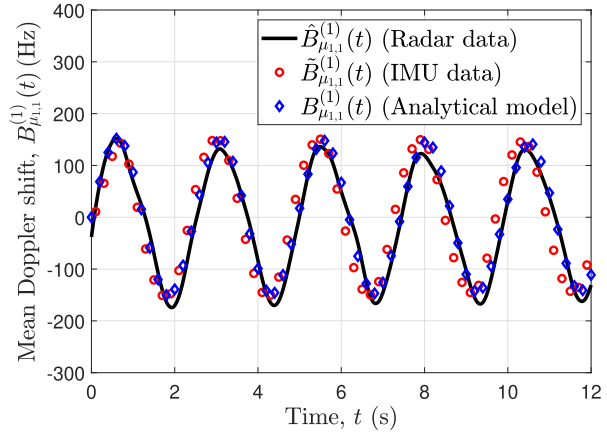

FIGURE 14. The TV mean Doppler shift of $B^{(1)}_{\mu_{1,1}}(t)$ of the A_1^T–A_1^R link.

the spectrograms in Figs. 10−13, an impact of the different antenna positions (MIMO links) on the frequency range of the TV mean Doppler shift can be observed in Figs. 14−17.

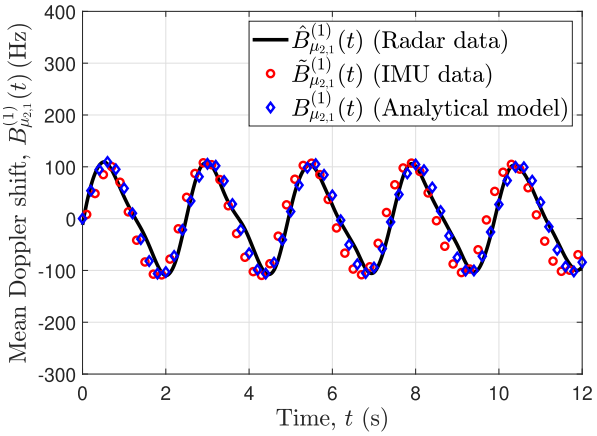

FIGURE 15. The TV mean Doppler shift $B^{(1)}_{\mu_{2,1}}(t)$ of the A_1^T–A_2^R link.

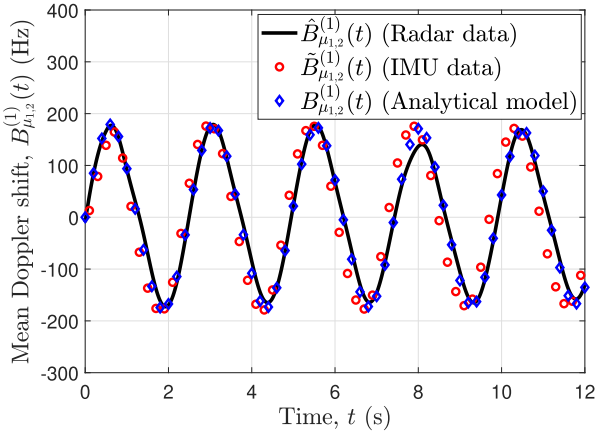

FIGURE 16. The TV mean Doppler shift $B^{(1)}_{\mu_{1,2}}(t)$ of the A_2^T–A_1^R link.

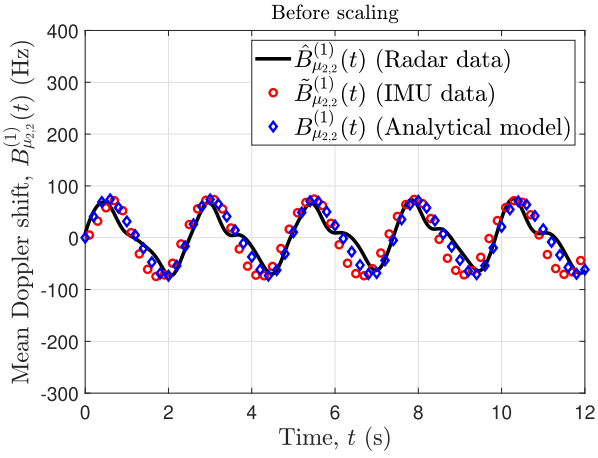

FIGURE 17. The TV mean Doppler shift $B^{(1)}_{\mu_{2,2}}(t)$ of the A_2^T–A_2^R link.

Furthermore, we can observe an excellent match between the TV mean Doppler shift of the measured channel, the IMU data-driven channel, and the analytical channel model. This confirms the usefulness of the proposed model for all MIMO links considering different antenna positions. As we mentioned earlier, we also conducted MOCAP data for the trajectories of the pendulum, while configuring the radar kit as

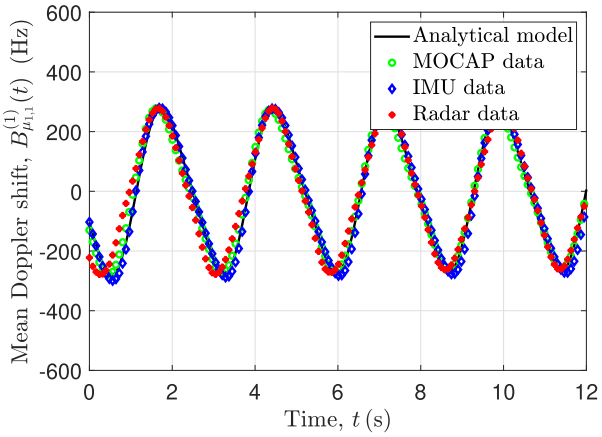

FIGURE 18. The TV mean Doppler shift $B^{(1)}_{\mu_{1,1}}(t)$ of the SISO channel.

a SISO system and activating the IMU sensor too. Fig. 18 shows the corresponding TV mean Doppler shift for this experiment. We can see that the results of all models exhibit an excellent agreement.

VI. CONCLUSION

In this paper, we have proposed a 3D trajectory-driven non-stationary mm-Wave MIMO channel model for a moving point scatterer. We have presented the TV-CTF capturing the effect of the mobility of the moving point scatterer. We have studied the TV Doppler characteristics of the proposed channel model, i.e., the TV Doppler spectrogram and the TV mean Doppler shift. The TV micro-Doppler signature of the proposed channel model has been validated by measured data, which are obtained by using a MIMO radar operating at 24 GHz. The obtained results have shown excellent agreement between the measured data and the proposed trajectory-driven channel model. Moreover, we have captured the TV trajectory of the pendulum by using both the IMU sensor and the QTM-based MOCAP camera system. The accuracy of the proposed non-stationary channel model has been confirmed by demonstrating a perfect match between the TV Doppler spectrograms of the measured (radar, IMU, MOCAP) data and the analytical model. We have also investigated the impact of the different MIMO links on the Doppler spectrogram of the received signal. The results demonstrate the importance of the antenna elements position for the analysis of the micro-Doppler signatures caused by the mobility of an object. Furthermore, the comparison analysis of the trajectories obtained from the MOCAP and IMU sensor data show that the MOCAP system outperforms the IMU sensor with respect to the analytical trajectory-driven model. It is important to obtain a set of data that can accurately replicate the fingerprints of real-life activities. We believe that our trajectory-driven channel model can serve as a basis for the derivation of a generic indoor channel model reproducing the Doppler characteristics caused by a moving point scatterer. As a future work, this model can be extended by considering multiple moving scatterers.

ACKNOWLEDGMENT

The authors would like to thank Mr. Ahmed Abdelgawwad for his assistance in performing the experiments and analysing the trajectories of the IMU data.

REFERENCES

[1] C.-X. Wang, J. Huang, H. Wang, X. Gao, X. You, and Y. Hao, "6G wireless channel measurements and models: Trends and challenges," *IEEE Veh. Technol. Mag.*, vol. 15, no. 4, pp. 22–32, Dec. 2020.
[2] S. Hur, S. Baek, B. Kim, Y. Chang, A. F. Molisch, T. S. Rappaport, K. Haneda, and J. Park, "Proposal on millimeter-wave channel modeling for 5G cellular system," *IEEE J. Sel. Topics Signal Process.*, vol. 10, no. 3, pp. 454–469, 2016.
[3] D. He, K. Guan, J. M. Garcia-Loygorri, B. Ai, X. Wang, C. Zheng, C. Briso-Rodríguez, and Z. Zhong, "Channel characterization and hybrid modeling for millimeter-wave communications in metro train," *IEEE Trans. Veh. Technol.*, vol. 69, no. 11, pp. 12408–12417, Nov. 2020.
[4] J. Huang, Y. Liu, C.-X. Wang, J. Sun, and H. Xiao, "5G millimeter wave channel sounders, measurements, and models: Recent developments and future challenges," *IEEE Commun. Mag.*, vol. 57, no. 1, pp. 138–145, Jan. 2019.
[5] S. Salous, S. M. Feeney, X. Raimundo, and A. A. Cheema, "Wideband MIMO channel sounder for radio measurements in the 60 GHz band," *IEEE Trans. Wireless Commun.*, vol. 15, no. 4, pp. 2825–2832, Apr. 2016.
[6] X. Zhao, S. Li, Q. Wang, M. Wang, S. Sun, and W. Hong, "Channel measurements, modeling, simulation and validation at 32 GHz in outdoor microcells for 5G radio systems," *IEEE Access*, vol. 5, pp. 1062–1072, 2017.
[7] J. Chen, X. Yin, X. Cai, and S. Wang, "Measurement-based massive MIMO channel modeling for outdoor LoS and NLoS environments," *IEEE Access*, vol. 5, pp. 2126–2140, 2017.
[8] T. S. Rappaport, G. R. Maccartney, M. K. Samimi, and S. Sun, "Wideband millimeter-wave propagation measurements and channel models for future wireless communication system design," *IEEE Trans. Commun.*, vol. 63, no. 9, pp. 3029–3056, Sep. 2015.
[9] K. Haneda, J. Järveläinen, A. Karttunen, M. Kyrö, and J. Putkonen, "A statistical spatio-temporal radio channel model for large indoor environments at 60 and 70 GHz," *IEEE Trans. Antennas Propag.*, vol. 63, no. 6, pp. 2694–2704, Jun. 2015.
[10] P. B. Papazian, K. A. Remley, C. Gentile, and N. Golmie, "A radio channel sounder for mobile millimeter-wave communications: System implementation and measurement assessment," *IEEE Trans. Microw. Theory Techn.*, vol. 64, no. 9, pp. 2924–2932, Sep. 2016.
[11] J. Ko, Y.-J. Cho, S. Hur, T. Kim, J. Park, A. F. Molisch, K. Haneda, M. Peter, D.-J. Park, and D.-H. Cho, "Millimeter-wave channel measurements and analysis for statistical spatial channel model in in-building and urban environments at 28 GHz," *IEEE Trans. Wireless Commun.*, vol. 16, no. 9, pp. 5853–5868, Sep. 2017.
[12] J.-J. Park, J. Lee, J. Liang, K.-W. Kim, K.-C. Lee, and M.-D. Kim, "Millimeter wave vehicular blockage characteristics based on 28 GHz measurements," in *Proc. IEEE 86th Veh. Technol. Conf. (VTC-Fall)*, Sep. 2017, pp. 1–5.
[13] M. Boban, D. Dupleich, N. Iqbal, J. Luo, C. Schneider, R. Müller, Z. Yu, D. Steer, T. Jämsä, J. Li, and R. S. Thomä, "Multi-band vehicle-to-vehicle channel characterization in the presence of vehicle blockage," *IEEE Access*, vol. 7, pp. 9724–9735, 2019.
[14] A. Maltsev, A. Pudeyev, I. Karls, I. Bolotin, G. Morozov, R. Weiler, M. Peter, and W. Keusgen, "Quasi-deterministic approach to mmWave channel modeling in a non-stationary environment," in *Proc. IEEE Globecom Workshops (GC Wkshps)*, Dec. 2014, pp. 966–971.
[15] Y. Zheng, Y. Zhang, K. Qian, G. Zhang, Y. Liu, C. Wu, and Z. Yang, "Zero-effort cross-domain gesture recognition with Wi-Fi," in *Proc. 17th Annu. Int. Conf. Mobile Syst., Appl., Services (MobiSys)*. New York, NY, USA: Association for Computing Machinery, Jun. 2019, pp. 313–325, doi: 10.1145/3307334.3326081.
[16] C. Gustafson, K. Haneda, S. Wyne, and F. Tufvesson, "On mm-wave multipath clustering and channel modeling," *IEEE Trans. Antennas Propag.*, vol. 62, no. 3, pp. 1445–1455, Mar. 2014.
[17] S. Alhloul and D. Richter, "Measuring the effects of object movement on the coherence bandwidth of indoor wireless channels at 2.6 GHz," in *Proc. IEEE 7th Annu. Inf. Technol., Electron. Mobile Commun. Conf. (IEMCON)*, Oct. 2016, pp. 1–5.

[18] M. G. Amin, Y. D. Zhang, F. Ahmad, and K. C. D. Ho, "Radar signal processing for elderly fall detection: The future for in-home monitoring," *IEEE Signal Process. Mag.*, vol. 33, no. 2, pp. 71–80, Mar. 2016.

[19] J. Bian, C.-X. Wang, M. Zhang, X. Ge, and X. Gao, "A 3-D non-stationary wideband MIMO channel model allowing for velocity variations of the mobile station," in *Proc. IEEE ICC*, May 2017, pp. 1–6.

[20] A. Abdelgawwad and M. Päetzold, "A 3D non-stationary cluster channel model for human activity recognition," in *Proc. IEEE 89th Veh. Technol. Conf. (VTC-Spring)*, Apr. 2019, pp. 1–7.

[21] J. Huang, C.-X. Wang, Y. Liu, J. Sun, and W. Zhang, "A novel 3D GBSM for mmWave MIMO channels," *Sci. China Inf. Sci.*, vol. 61, no. 10, Oct. 2018, Art. no. 102305.

[22] M. Mohamed, M. Cheffena, F. P. Fontan, and A. Moldsvor, "A dynamic channel model for indoor wireless signals: Working around interference caused by moving human bodies," *IEEE Antennas Propag. Mag.*, vol. 60, no. 2, pp. 82–91, Apr. 2018.

[23] Q. Zhu, Y. Yang, C.-X. Wang, Y. Tan, J. Sun, X. Chen, and W. Zhong, "Spatial correlations of a 3-D non-stationary MIMO channel model with 3-D antenna arrays and 3-D arbitrary trajectories," *IEEE Wireless Commun. Lett.*, vol. 8, no. 2, pp. 512–515, Apr. 2019.

[24] R. S. A. R. Abdullah, A. Alnaeb, A. A. Salah, N. E. A. Rashid, A. Sali, and I. Pasya, "Micro-Doppler estimation and analysis of slow moving objects in forward scattering radar system," *Remote Sens.*, vol. 9, no. 699, pp. 1–23, Jul. 2017.

[25] A. Abdelgawwad, A. Borhani, and M. Pätzold, "Modelling, analysis, and simulation of the micro-Doppler effect in wideband indoor channels with confirmation through pendulum experiments," *Sensors*, vol. 20, no. 4, pp. 1–18, Feb. 2020.

[26] N. Avazov, R. Hicheri, and M. Pätzold, "A trajectory-driven SIMO mm-wave channel model for a moving point scatterer," in *Proc. 15th Eur. Conf. Antennas Propag. (EuCAP)*, Mar. 2021, pp. 1–5.

[27] *Sensors for Motion Capture, Biomechanics, Industrial Control, Robotics, Facility Management, Cold Storage, Research, and Product Development*. Accessed: Aug. 15, 2021. [Online]. Available: https://mbientlab.com/

[28] A. R. Jensenius, K. Nymoen, S. A. Skogstad, and A. Voldsund, "A study of the noise-level in two infrared marker-based motion capture systems," in *Proc. 9th Sound Music Comput. Conf.*, Copenhagen, Denmark, Jul. 2012, pp. 1–6.

[29] X. Yun, E. R. Bachmann, H. Moore, and J. Calusdian, "Self-contained position tracking of human movement using small inertial/magnetic sensor modules," in *Proc. IEEE Int. Conf. Robot. Autom.*, Apr. 2007, pp. 2526–2533.

[30] Qualisys. (2021). *Motion Capture Systems*. Accessed: Mar. 24, 2021. [Online]. Available: https://www.qualisys.com/

[31] (2021). *Miqus Hybrid*. Accessed: Mar. 24, 2021. [Online]. Available: https://www.qualisys.com/cameras/miqus-hybrid/

[32] (2021). *Qualisys Track Manager (QTM)*. Accessed: Mar. 24, 2021. [Online]. Available: https://www.qualisys.com/software/qualisys-track-manager/

NURILLA AVAZOV (Member, IEEE) received the B.Sc. and M.Sc. degrees in telecommunications from Tashkent University of Information Technologies, Uzbekistan, in 2005 and 2007, respectively, and the Ph.D. degree in telecommunications engineering from the University of Agder, Norway, in 2015. From 2016 to 2017, he was with the UWB Wireless Communications Research Center, Inha University, as a Postdoctoral Researcher. From 2017 to 2020, he was with the School of Computer Science, The University of Auckland, New Zealand. He is currently working as a Postdoctoral Research Fellow with the University of Agder. He has authored or coauthored numerous technical papers in various journals and conferences. His research interests include wireless communications, stochastic and deterministic channel modeling, machine learning, time series data analysis, and applications of machine learning in wireless communications and services.

RYM HICHERI (Member, IEEE) was born in Tunis, Tunisia, in 1988. She received the D.P.C.U. degree from the Institut Préparatoire Aux Etudes d'Ingénieurs d'El Manar, in 2009, and the Eng. degree in telecommunications and the Ph.D. degree in information and communication technology from the Ecole Supérieure des Communications de Tunis, in 2012 and 2017, respectively. She is currently a Postdoctoral Research Fellow with the University of Agder, Norway. Her current research interests include channel modeling, wireless communications, estimation and optimization, and information theory.

MUHAMMAD MUAAZ received the M.Sc. degree in information and communication systems security from the KTH Royal Institute of Technology, Sweden, and the Ph.D. degree in computer science from Johannes Kepler University, Austria. From 2018 to 2020, he worked as a Postdoctoral Fellow with the University of Agder, Norway, where he is currently working as a Scientific Researcher. His research interests include information security, data analysis, machine learning, deep learning, biometrics, and human behavior, and activity recognition.

FILIPPO SANFILIPPO (Senior Member, IEEE) received the Ph.D. degree in engineering cybernetics. He is currently an Associate Professor with the Department of Engineering Sciences, Faculty of Engineering and Science, University of Agder (UiA), Grimstad, Norway. He is also appointed as a Professor II with the Department of Mechanical, Electronic and Chemical Engineering, Faculty of Technology, Art and Design, Oslo Metropolitan University (OsloMet), Oslo, Norway. He is responsible for the research theme on Collaborative Robots (CoBots) with the Top Research Centre Mechatronics, UiA, where he is also a member of the Centre for Integrated Emergency Management (CIEM). He has authored or coauthored several technical papers in various journals and conferences. His research interests include robotics, wearable haptics, and safe human–robot interaction. He is currently supervising four Ph.D. students and co-supervising one postdoctoral student. He carries experience in participating in European Research Programs and various national projects from the Research Council of Norway (RCN). He is currently the Chair of the IEEE Norway Section. He is also the Chair of the IEEE Robotics and Automation, Control Systems and Intelligent Transportation Systems Joint Chapter. He is also the Treasurer of the Norsk Forening for Kunstig Intelligens (NAIS), the Norwegian Association for Artificial Intelligence. He is a reviewer for several international conferences and journals.

MATTHIAS PÄTZOLD (Senior Member, IEEE) received the Dipl.-Ing. and Dr.-Ing. degrees in electrical engineering from Ruhr-Universität Bochum, Bochum, Germany, in 1985 and 1989, respectively, and the habilitation degree in communications engineering from Hamburg University of Technology, Hamburg, Germany, in 1998. From 1990 to 1992, he was with ANT Nachrichtentechnik GmbH, Backnang, Germany, where he was involved in digital satellite communications. From 1992 to 2001, he was with the Department of Digital Networks, Hamburg University of Technology. Since 2001, he has been a Full Professor of mobile communications with the University of Agder, Norway. He has authored several books and numerous technical papers. He has been actively participating in numerous conferences serving as a TPC member and the TPC chair. His publications received 14 best paper awards.